

## Solid-state experiments at high pressure and strain rate\*

D. H. Kalantar,<sup>†,a)</sup> B. A. Remington, J. D. Colvin, K. O. Mikaelian, S. V. Weber,  
and L. G. Wiley

*Lawrence Livermore National Laboratory, Livermore, California 94550*

J. S. Wark, A. Loveridge, and A. M. Allen

*Department of Physics, Clarendon Laboratory, University of Oxford, Oxford, OX1 3PU, United Kingdom*

A. A. Hauer

*Los Alamos National Laboratory, Los Alamos, New Mexico 87545*

M. A. Meyers

*University of California at San Diego, La Jolla, California 92093*

(Received 15 November 1999; accepted 28 January 2000)

Experiments have been developed using high powered laser facilities to study the response of materials in the solid state under extreme pressures and strain rates. Details of the target and drive development required for solid-state experiments and results from two separate experiments are presented. In the first, thin foils were compressed to a peak pressure of 180 GPa and accelerated. A pre-imposed modulation at the embedded Rayleigh–Taylor unstable interface was observed to grow. The growth rates were fluid-like at early time, but suppressed at later time. This result is suggestive of the theory of localized heating in shear bands, followed by conduction of the heat into the bulk material, allowing for recovery of the bulk material strength. In the second experiment, the response of Si was studied by dynamic x-ray diffraction. The crystal was observed to respond with uni-axial compression at a peak pressure 11.5–13.5 GPa. © 2000 American Institute of Physics. [S1070-664X(00)94505-1]

### I. INTRODUCTION

The dynamics of material response to pressure loading depends on the pressure and strain rate. Processes may be extremely slow, such as the movement of the tectonic plates on the earth ( $10^{-17}$ – $10^{-14}$  s<sup>-1</sup>),<sup>1</sup> or fast, such as the dynamic response of materials under shock loading ( $10^3$ – $10^7$  s<sup>-1</sup> or higher).<sup>2</sup> There are experimental techniques that allow us to access these different regimes. The diamond anvil cell is an example for slow isotropic compressions up to the 100 GPa (1 Mbar) range (limited by strength of the press itself). For dynamic processes, there are Hopkinson bar test facilities, gun facilities, and high-explosive (HE) facilities. In these, the pressures are typically <100 GPa, and only moderate strain rates ( $10^3$ – $10^6$  s<sup>-1</sup>) are accessed. The response of a metal under extreme pressure (>100 GPa) and high-strain rate (> $10^7$  s<sup>-1</sup>) is typically inferred by extrapolation from experiments that are done at lower pressures (<100 GPa) and moderate strain rates ( $10^6$  s<sup>-1</sup>).

One model used to describe material response under shock loading is the Steinberg–Guinan constitutive model.<sup>3</sup> This is a semiempirical strain-rate independent model for the shear stress and yield stress

$$G(P, T) = G_o \left[ 1 + \left( \frac{G'_P}{G_o} \right) \frac{P}{\eta^{1/3}} + \left( \frac{G'_T}{G_o} \right) (T - 300) \right], \quad (1a)$$

$$Y(P, T) = Y_o [1 + \beta(\varepsilon + \varepsilon_i)]^n$$

$$\times \left[ 1 + \left( \frac{G'_P}{G_o} \right) \frac{P}{\eta^{1/3}} + \left( \frac{G'_T}{G_o} \right) (T - 300) \right] \quad (1b)$$

where  $G$  is the shear modulus,  $Y$  is the yield strength,  $\varepsilon$  is the strain, and  $\eta$  is the compression. The pressure ( $P$ ) and temperature ( $T$ ) derivatives of  $G$  are represented by  $G'_P$  and  $G'_T$  respectively. This model is an elastic-perfectly plastic model. When a stress is applied to a sample, it responds elastically up to the point where the stress exceeds the yield stress. At that point, it yields to plastic flow. This formulation includes the enhancement of strength due to pressure and work hardening ( $\beta$ ), and softening due to temperature.

In fact the material has a lattice structure is not taken into account in such an empirical description. When the solid undergoes deformation at high pressure, stresses result in the generation and subsequent propagation of lattice dislocations.<sup>4</sup> Solid-state plastic flow is caused by the rearrangement of the lattice structure by transport of these dislocations.

The number density of dislocations that are generated and the speed with which they propagate depend on the rate of the applied strain. The parameters defined in the constitutive materials model<sup>3</sup> are determined from experiments at pressures below 100 GPa and strain rates on the order of  $10^3$ – $10^6$  s<sup>-1</sup>. Application of the model is speculative at the higher strain rates of  $10^7$ – $10^9$  s<sup>-1</sup> that may be achieved with a laser driven shock experiment. As a result, it is important to characterize the shock response of materials at high pres-

\*Paper B11 5 Bull. Am. Phys. Soc. **44**, 19 (1999).

<sup>†</sup>Invited speaker.

<sup>a)</sup>Electronic mail: kalantar1@llnl.gov

tures and strain rates in order to evaluate the validity of materials models such as the model of Steinberg *et al.*<sup>3</sup>

Intense lasers have been used for high-pressure fluid hydrodynamics experiments and equation of state experiments relevant to inertial confinement fusion and to laboratory astrophysics. The laser provides a source of high energy density that may be used to launch shocks that are up to  $10^5$  GPa for fluid experiments. With appropriate target and laser pulse shape, materials may be compressed at more moderate pressures ( $>100$  GPa) while remaining solid. This allows solid-state experiments to be done in regimes of very high pressure and strain rate

In this paper we describe the experimental technique for performing solid-state experiments using an intense laser. We present details of the target design, and drive characterization, along with calculations of the state of the material. We show results from Rayleigh–Taylor (RT) instability experiments using thin Al foils, and we also discuss dynamic diffraction experiments probing the lattice response of shock compressed Si crystals.

## II. ALUMINUM INSTABILITY EXPERIMENT

In a classical fluid model, when a light fluid accelerates a heavier fluid, the interface is RT unstable. A mass modulation at the embedded material interface is unstable, and can grow under acceleration. In the solid state, however, the strength of the material can counter the effect of the RT instability. The parameters that define whether a material is stable or unstable to instability growth in the solid state depend on the wavelength and amplitude of the modulation, the acceleration, foil thickness, and material properties, such as yield stress, and shear modulus.

The effect of strength on instability growth in the plastic flow regime has been investigated by Barnes *et al.*<sup>5</sup> using Al plates that have a pre-imposed surface modulation. The Al plates were driven with a shockless HE drive. Similar experiments were done by Lebedev *et al.*,<sup>6,7</sup> using Al and Ti plates. We are conducting experiments on the Nova laser<sup>8</sup> to study the plastic flow of metals at high-pressure and very high-strain rates. Thin foils of Al are compressed by a factor of 1.5–2.0 with staged shocks reaching peak pressures of up to 180 GPa. The Rayleigh–Taylor instability is the observable “probe” in this experiment, with departures from classical (liquid) behavior characterizing the material strength properties at high pressure and compression.

In order to perform such a solid-state experiment, the sample must be compressed nearly isentropically such that the final temperature is below the material melt temperature. This is achieved in the Nova hydrodynamics experiments using an x-ray drive created in a cylindrical gold hohlraum. The target geometry is shown in Fig. 1. The hohlraum [Fig. 1(a)] is cylindrically symmetric, 3.44 mm in diameter, and 5.75 mm long. The hydrodynamics package is mounted on the side of the hohlraum at the midplane.

Eight Nova beams enter the hohlraum through the laser entrance holes and are incident on the inner wall of the two laser heated cavities of the target. The high-intensity laser ionizes the surface of the *Hohlraum* wall to create a plasma,

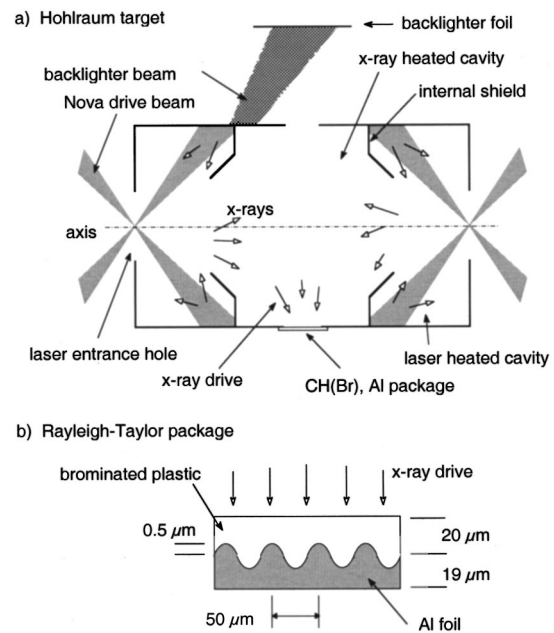


FIG. 1. (a) *Hohlraum* target configuration showing the laser heated cavities, the x-ray heated cavity, and the internal shields to block x-ray preheating of the foil package. (b) Cross section of a typical RT instability package consisting of a CH(Br) ablator and modulated Al foil.

and the laser energy is absorbed by inverse bremsstrahlung. X-rays that are re-emitted from the wall pass through the holes in the internal shields to heat the central (x-ray heated) cavity and ablate material from the surface of the package. This launches a series of shocks to compress the package and accelerate it away from the hohlraum. The internal shields shown in Fig. 1 prevent preheating of the package by hard x-rays generated at the laser spots.

The Al foil package consists of a  $20\ \mu\text{m}$  thick brominated polystyrene [CH(Br)] ablator pressed in contact with the Al foil [Fig. 1(b)]. We typically use Al-6061 foils that have been rolled and then machined to have a sinusoidal modulation and an average thickness of  $18\text{--}20\ \mu\text{m}$ .

A purely isentropic compression may be achieved with a pressure pulse that rises slowly so that a shock cannot form in the material during the experiment. This is approximated in the laser experiment using two shocks. An 8.5 ns long laser pulse shape is created by temporally staggering the eight drive beams so that they enter the hohlraum in pairs (Fig. 2). A total of  $\sim 14$  kJ of  $0.35\ \mu\text{m}$  wavelength laser energy is deposited into the hohlraum. This generates an x-ray drive pressure that launches the two shocks to compress and accelerate the foil away from the side of the hohlraum.

We have characterized the x-ray drive in the central cavity of the hohlraum using the Dante diagnostic<sup>9</sup> and side-on foil trajectories. The Dante diagnostic is an array of absolutely calibrated filtered x-ray detectors. This provided a measurement of the radiation temperature as a function of time. We have also performed simulations of the drive inside the hohlraum to establish a detailed model for the drive history.

The peak portion and the late time decay of the drive

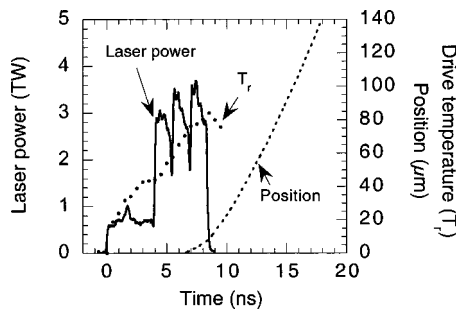


FIG. 2. Laser pulse shape used for the Al RT experiment. The resulting x-ray drive temperature and simulated foil trajectory are shown overlaid.

are verified with side-on foil trajectory measurements of an Al foil. The back surface of the Al foil moves  $\sim 140 \mu\text{m}$  after 18 ns. The drive history and calculated trajectory of the rear (free) surface of the foil are shown overlaid in Fig. 2.

The conditions in the Al foil are calculated at the embedded interface with the one-dimensional (1D) simulations using the radiation-hydrodynamics code LASNEX.<sup>10</sup> The calculated temperature and pressure at the embedded ablator–Al interface are shown in Fig. 3. Two shocks are created, the first at a pressure of 20–30 GPa and the second at a pressure of 180 GPa (1.8 Mbar), as shown in Fig. 3(a). The Atwood number is about 0.13 from 6 to 13 ns, and then it increases to 0.2. The time scale of this experiment is short, and the longitudinal strain rate is about  $7 \times 10^7 \text{ s}^{-1}$ . The slow decay of the hohlraum x-ray drive maintains the high pressure until about 10 ns. During the experiment, the interface accelerates to a velocity of about  $16 \mu\text{m/ns}$  at 20 ns. In these simulations, the material temperature at the interface stays below the melt temperature, which we calculate by the Lindemann law as described in Ref. 11

$$T_m = T_{mo} \exp\{2a(1 - 1/\eta)\} \eta^{2(\gamma_o - n - 1/3)}, \quad (2)$$

where  $T_{mo}$  is the melt temperature at constant volume,  $\eta$  is the volume compression of the sample,  $\gamma$  is the Grüneisen gamma, and  $a$  is the coefficient of volume dependence of  $\gamma$ , as defined by Steinberg *et al.*<sup>3</sup>

This drive is calculated to keep the foil very near the conditions of an isentropic compression throughout the experiment. In Fig. 3(b) we show the internal energy at the Al interface plotted as a function of density (compression) from  $t=0$  to  $t=15$  ns. The dotted curve labeled “isentropic” here

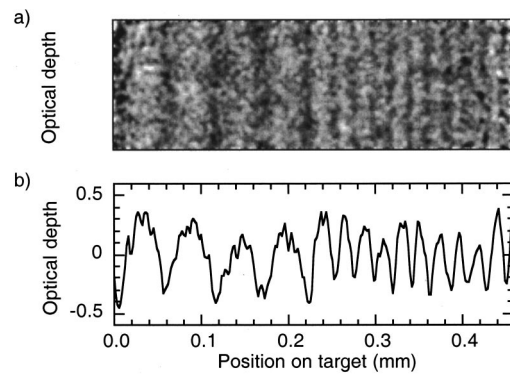


FIG. 4. (a) Sample x-ray radiograph of an Al foil with 50 and 20  $\mu\text{m}$  wavelength perturbations. This is shown as modulation in optical depth for the 4.3 keV probe x-rays. (b) Lineout of optical depth modulation.

corresponds to an isentropic compression, the solid curve represents the principle Hugoniot, and the dot–dashed curve corresponds to the melt curve.

### III. INSTABILITY GROWTH EXPERIMENTS

As the foil is accelerated, preimposed sinusoidal modulations of wavelengths 10, 20, and 50  $\mu\text{m}$  and initial amplitude 0.5  $\mu\text{m}$  grow due to the Rayleigh–Taylor instability. This perturbation growth is diagnosed using x-rays generated by two additional beams on Nova which are incident with a 4 ns square pulse on a separate Sc backlighter foil with a large area (0.7 mm diam) focal spot to generate  $\text{He}_\alpha$  x-rays at 4.3 keV. Two-dimensional images of the x-ray transmission through the modulated foil are recorded using a gated x-ray imager (FXI) using 5  $\mu\text{m}$  pinholes at 12 times magnification.<sup>12,13</sup> Up to 16 images are recorded on four independently timed microchannel plate striplines on each laser shot using a 230 ps wide gate pulse. A typical image is shown in Fig. 4, displayed in optical depth of the foil. A lineout of the modulation in optical depth [Fig. 4(b)] is analyzed to extract the Fourier amplitude at the modulation wavelength. This is then normalized to the initial contrast in optical depth, thereby effectively removing the instrument resolution from the measurement. Note that the instrument modulation transfer function is about 0.6 at  $12\times$  for  $\lambda=20\mu\text{m}$ .

The measured growth factors for the three perturbation wavelengths are shown in Fig. 5. Each point represents the results from up to four images on a single stripline of the

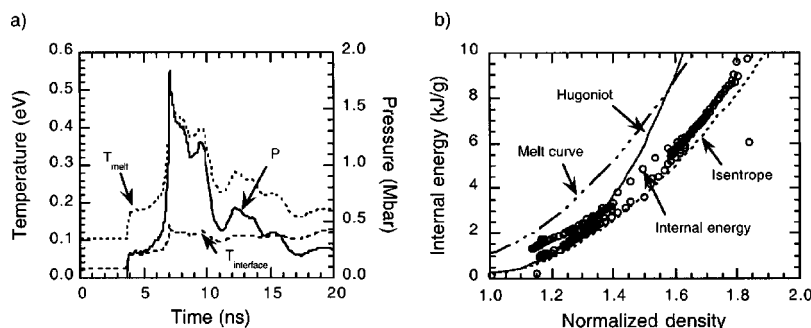


FIG. 3. (a) Pressure and temperature history at the embedded interface for a shocked Al foil. The melt temperature calculated by the Lindemann melt law is overlaid. (b) Internal energy trajectory calculated for the embedded Al interface. This is shown with the melt curve, shock hugoniot, and an isentrope.

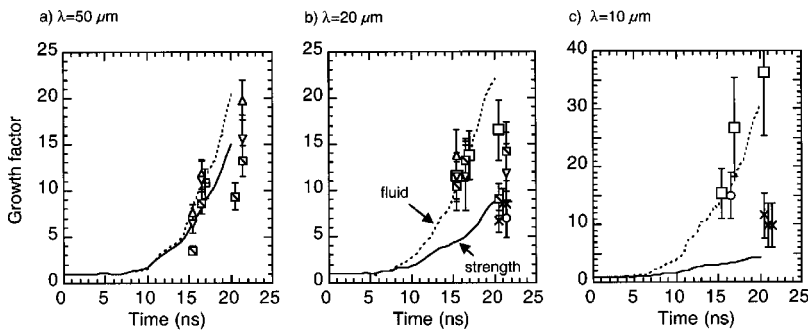


FIG. 5. Measured perturbation amplitude shown plotted as growth factors above the initial pre-imposed amplitude for the Al RT instability experiments: (a) 50  $\mu\text{m}$  modulation, (b) 20  $\mu\text{m}$  modulation, and (c) 10  $\mu\text{m}$  modulation. Each shot is represented by a different symbol, and data at two different wavelengths from the same shot are shown with the same symbol.

gated microchannel plate. The error bars represent the statistical error in the mean for the collection of images. In cases where there were only one or two images, the error bar represents the amplitude of the noise of neighboring modes in Fourier space relative to that of the pre-imposed single mode.

Overlaid on the graphs, we have plotted the simulated growth factors using both a fluid model (i.e., no material strength) (dashed curve), and the constitutive material strength model described by Steinberg *et al.* (solid curve). These simulations are fully two-dimensional, including any nonlinear hydrodynamic growth. Values of the model parameters used were  $Y_o = 0.29$  GPa,  $G_o = 27.6$  GPa,  $\beta = 125$ , and  $n = 0.10$ . The data show variation from shot to shot, but a trend emerges. At about 15–16 ns, the growth factors are consistent with fluid growth. However, at later times (20–22 ns), the perturbations generally have not grown as much as we calculate using the fluid models. This suggests that there may be a time-dependent saturation or stabilization mechanism affecting the instability growth. Simulations of the fluid growth of shorter wavelength modes characteristic of the initial surface finish indicate negligible coupling to the pre-imposed mode, and that growth from fine-scale surface finish modes does not lead to the reduced growth at late time for  $\lambda = 10$  and  $20 \mu\text{m}$ . We conjecture that the saturation or stabilization is due to a time-dependent material strength effect, as is discussed below.

**IV. STRENGTH STABILIZATION**

The initial values for yield strength and shear modulus for bulk Al-6061 are  $Y_o = 0.29$  GPa and  $G_o = 27.6$  GPa, re-

spectively. At a shock pressure of 180 GPa, the Al foil is compressed by about a factor of 1.7–1.8, at which point the yield strength is 3.3 GPa, enhanced by more than a factor of 10 over the nominal value,  $Y_o$ . The applied stress (pressure) exceeds the yield strength by more than an order of magnitude, putting the foil into the plastic flow regime and allowing for instability growth in the solid state.

Estimates can be made as to whether the modulation on the Al package grows or not, based on a steady-state stability boundary analysis. Lebedev *et al.*<sup>6</sup> provide an expression defining stability boundary as a function of both the amplitude and the wavelength of the modulation

$$\eta_c = \eta_c(\text{Drucker}) [1 - 0.86e^{(-2\pi H/\sqrt{3}\lambda)}] \times \left\{ [1 - e^{(-2\pi H/\sqrt{3}\lambda)}]^2 - \left(\frac{\lambda}{\lambda_\infty}\right)^2 \right\}, \tag{3}$$

where  $H$  is the thickness of the sample

$$\lambda_\infty = 4\pi G/\rho g, \tag{4}$$

is the cut-off wavelength for a semi-infinite sample from Miles<sup>14</sup> and

$$\eta_c(\text{Drucker}) = \frac{2Y}{\rho g}, \tag{5}$$

is the wavelength independent critical amplitude threshold for instability growth from Drucker.<sup>15</sup> Note that  $\rho$  is the density, and  $g$  is the acceleration. For a given set of conditions ( $Y, G, H, g, \rho$ ), wavelengths  $\lambda$  are predicted to be stable if  $\eta < \eta_c$  in this model.

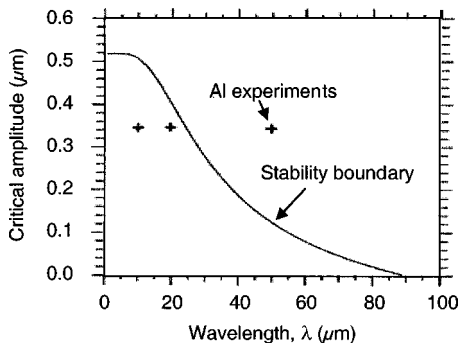


FIG. 6. Stability boundary calculated Al RT instability experiment calculated with average conditions at 8–12 ns.

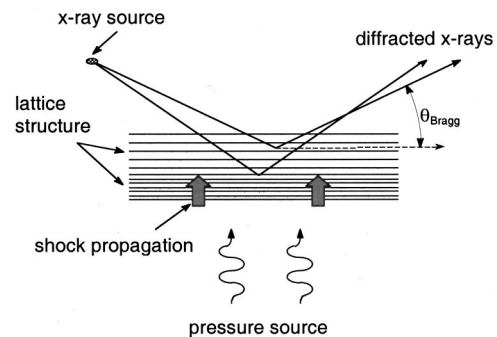


FIG. 7. Illustration of dynamic x-ray diffraction being applied to probe lattice compression of a shocked sample.

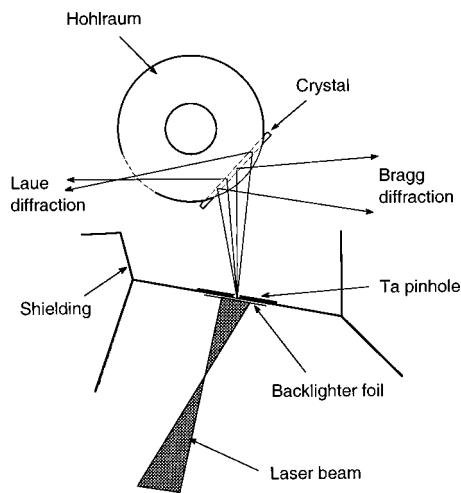


FIG. 8. Diagram of the *Hohlräum* target configuration for dynamic x-ray diffraction measurements.

For average conditions at 8–12 ns, the stability curve predicted by Eq. (3) is shown in Fig. 6. The initial perturbation amplitudes are  $0.5 \mu\text{m}$ , but under shock compression these reduce to about  $0.35 \mu\text{m}$ . For wavelengths  $\lambda < 25 \mu\text{m}$ , the perturbations are predicted to be stabilized. Longer wavelengths are predicted to grow. Stabilization of perturbations with  $\lambda < 25 \mu\text{m}$  assumes there is no growth throughout. However, we observe growth that appears fluid-like at early times for all wavelengths, but appears to stagnate at late times for  $\lambda \leq 20 \mu\text{m}$ .

One possible explanation for this behavior is that the foil is responding nearly fluid-like due to thermal softening in localized shear regions, and then it regains strength as the heat conducts into the bulk material. This model is described by Grady and Asay.<sup>16</sup> As the energy stored in shear stress in the lattice dissipates in narrow regions (shear bands), large numbers of dislocations may be generated and the bulk sample may deform plastically. Grady and Asay have measured the size and spacing of shear bands observed in Al shock loading experiments at strain rates up to  $10^7 \text{ s}^{-1}$ . The thermal conduction time is on the order of 10 ns, consistent with the time scale over which we observe recovery of the strength in the RT instability experiments.

Although there is no explicit model to predict the response of a foil with shear band softening and subsequent

recovery of strength, this scenario offers a qualitative explanation for the RT growth history. Results from the experiments presented here are qualitatively similar to those of HE driven Al plate experiments of Rayevsky *et al.*<sup>17</sup> There, when the plate experiences shock loading, the perturbation growth is nearly fluid-like at early times, but appears to saturate later.

## V. DYNAMIC X-RAY DIFFRACTION

In order to develop a full understanding of a solid-state experiment such as the RT instability experiment described above, details of the response of the lattice are required. When the solid undergoes deformation at high pressure, stresses that occur at a lattice level result in the generation and subsequent propagation of dislocations<sup>18</sup> and localized shear bands.<sup>16</sup> Plastic material flow is the rearrangement of the lattice structure by transport of these dislocations. The number density of dislocations that are generated and the speed with which they propagate depend on the rate of the applied strain.

The technique of Bragg x-ray diffraction is being developed as a microscopic lattice diagnostic for laser driven solid-state experiments.<sup>19–22</sup> This technique provides a time-resolved measurement of the 2d lattice spacing. Here, x-rays of wavelength scattered from the atoms in the lattice constructively interfere when the incident angle with respect to the lattice plane satisfies the Bragg condition

$$n\lambda = 2d \times \sin(\theta). \quad (6)$$

The x-rays are diffracted at an angle  $\theta$  (relative to the lattice planes) (Fig. 7).

When the lattice undergoes a deformation due to shock compression, the lattice compresses, so the lattice spacing decreases. The Bragg diffraction condition is then met at a different angle determined by the new lattice spacing as illustrated schematically in Fig. 7. The shift in diffraction angle is recorded as a spatial shift in the diffraction signal.

Since the x-rays that are typically used for Bragg diffraction are multi-keV, the depth in the crystal that can be probed may be tens of microns. If there is a range of densities and corresponding lattice spacings within this depth of the surface, we record a Bragg diffracted signal from the

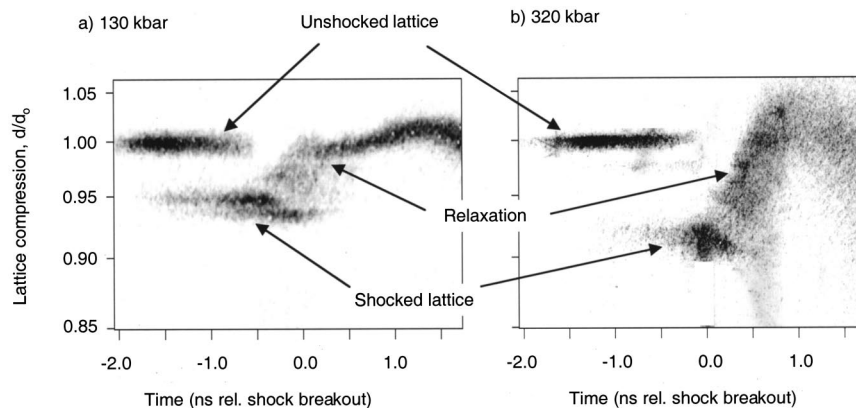


FIG. 9. Time-resolved x-ray diffraction data recorded from shock compressed Si (111) at pressures of (a) 13 GPa and (b) 32 GPa.

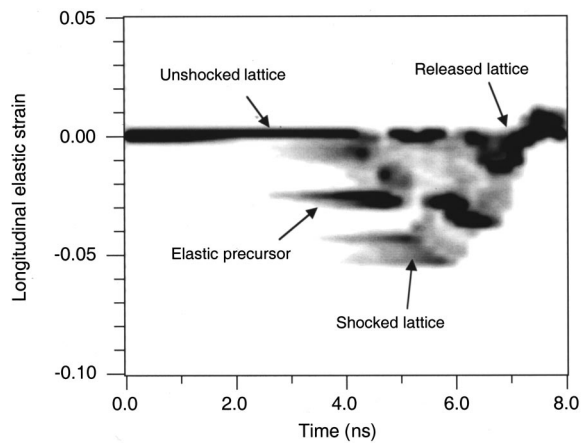


FIG. 10. Simulated x-ray diffraction from Si (111) shock compressed to 13 GPa. This is shown as longitudinal elastic strain as a function of time.

corresponding range of angles. In other words, we record a measure of the fraction of the material that is compressed at each density. In the absence of phase transitions, this technique can provide a measurement of the shock wave profile.<sup>23</sup>

Previously, dynamic x-ray diffraction has been done on laser driven LiF and Si crystals.<sup>20,24</sup> Additional experiments have been done with KCl and LiF shock compressed with an impactor on a powder gun facility.<sup>25,26</sup> We have done experiments to study shock compressed single crystal Si as a way to develop the technique for our laser experiments, with the eventual goal of characterizing the lattice response of the shocked Al samples used for RT instability experiments.

Up to eight beams of Nova are incident in the cylindrical gold hohlraum target shown in Fig. 1(a) to generate a Planckian soft x-ray drive. A Si crystal sample is mounted over the hole in the side of the hohlraum at the midplane. The crystal is  $1 \times 2$  mm in size and  $40 \mu\text{m}$  thick. It was cut for different experiments with a (111) or (100) orientation.

A 4 ns square laser pulse shape is used to drive a single shock in the Si. Two additional beams of Nova are used to generate the x-ray source for Bragg diffraction. These beams are pointed onto a thin ( $5 \mu\text{m}$ ) V or Fe foil that was masked with a Ta pinhole aperture (Fig. 8) to provide a small ( $100 \mu\text{m}$ ) source of K-shell line emission. The emission from this

backlighter source is self filtered by the foil itself to provide a nearly mono-energetic backlighter spectrum.

The backlighter foil is located close to the crystal so that the crystal subtends an angle of up to about  $25^\circ$  to the x-ray source, allowing for a range of Bragg diffraction angles. The x-rays diffracted from the crystal are recorded with an x-ray streak camera. This camera is located with the photocathode only 12 cm from the target to collect nearly a  $15^\circ$  range of diffraction angles from the target. A film holder is located in front of the streak camera. It records a time-integrated record of the diffracted x-rays to complement the streak record. A second film holder was located on the opposite side to record the x-rays diffracted from the orthogonal lattice planes [(040) lattice planes] in the case of the Si (100) shock experiments.

## VI. DRIVE SCALING OF Si (111)

Silicon at ambient pressure is a diamond cubic lattice. The 2D spacing for the (111) lattice planes is  $6.27 \text{ \AA}$ . The Bragg angle for V He $_{\alpha}$  x-rays at  $2.38 \text{ \AA}$  is  $22.3^\circ$ . We recorded the diffracted signal from the (111) lattice planes at a range of drive pressures from 13 to 32 GPa, above the Hugoniot Elastic Limit (HEL) for Si (111), which is 5.4 GPa. Figure 9 shows the time-resolved diffraction signal recorded from the free surface of Si (111) shock compressed to 13 GPa [Fig. 9(a)] and 32 GPa [Fig. 9(b)]. These streaks are labeled to indicate compression as a function of time.

The streak records show a diffraction peak corresponding to the nominal (uncompressed) lattice spacing until the time the shock reaches the free surface, at which point the crystal is fully compressed and the static diffraction peak disappears. An additional diffraction peak corresponding to the compressed lattice is also visible. At shock breakout, the lattice releases, and the diffraction pattern shows an intermediate compression due to the dynamics of the release and a return to the initial lattice spacing. For the lower pressure case, the lattice is maintained for a long time following the release, though at a lattice spacing slightly larger than the initial spacing, presumably due to thermal expansion. However, for the higher-pressure case, the diffracted signal becomes more diffuse at late time following the shock breakout, indicating the crystal structure may be lost.

We are able to reproduce many of the features in the diffraction pattern using the LASNEX hydrodynamics code.

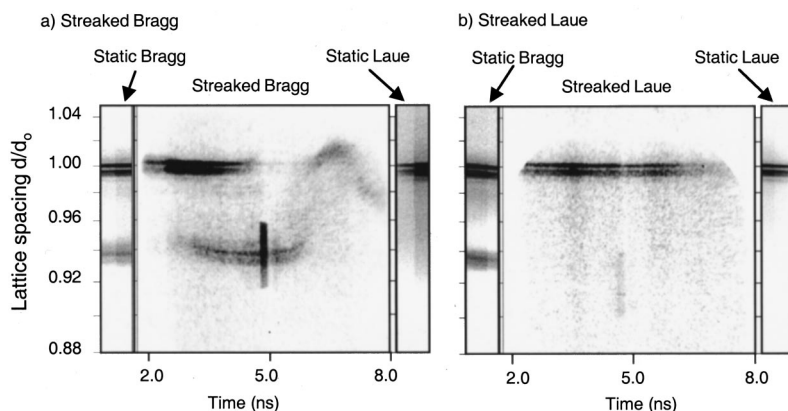


FIG. 11. Time-integrated and time-resolved data showing simultaneous diffraction from (400) and (040) lattice planes in Si shocked along the (400) direction at 11.5–13.5 GPa. (a) shows the static Bragg and Laue and streaked Bragg diffracted signals from one shot; (b) shows static Bragg and Laue and streaked Laue diffracted signals from a separate shot.

This is illustrated in Fig. 10, where we show a plot of the longitudinal elastic strain, displayed as a function of time for the case of Si (111) shocked to a peak pressure of 13 GPa. Diffraction from the unshocked and shocked lattice are shown, as well as the appearance of intermediate compression as the material releases. This simulation also shows a diffraction peak due to the elastic precursor wave, which we do not observe in the experiment. Such a simulation does not include the presence of the lattice and associated lattice dynamics. Molecular-dynamics simulations are required to provide more insight into the lattice response.<sup>27,28</sup>

## VII. MEASUREMENTS OF ORTHOGONAL PLANES OF SILICON (100)

An Fe backlighter foil provided He $\alpha$  x-rays of wavelength 1.85 Å, which diffract from the uncompressed (400) lattice planes at a Bragg angle of 42.95°. The crystal was shocked at 11.5–13.5 GPa along the (400) direction, and we recorded diffracted x-rays from the (400) (Bragg) and (040) (Laue) lattice planes simultaneously (Fig. 8). Note that for Si (400), the HEL is ~8.4 GPa. In Fig. 11 we show the data from two separate Nova shots. In the first case [Fig. 11(a)], we recorded the Bragg diffraction on static film (integrated over the duration of the backlighter pulse) and also with an x-ray streak camera. The Laue diffraction was recorded only on static x-ray film. For the second shot [Fig. 11(b)], the Laue diffraction was recorded with the streak camera.

The Bragg diffraction signal shows two strong peaks. One corresponds to diffraction from the uncompressed lattice. This is labeled to indicate fractional 1D compression normalized to the initial (400) lattice spacing as a function of time. We observe diffraction from the uncompressed Si, and also from shock compressed Si as the shock propagates toward the free surface of the crystal. The lattice is compressed in the shock direction by 6%. As the shock breaks out at the back surface, the crystal is fully compressed and the signal from the unshocked material disappears. The rarefaction returns the crystal to the initial density, characterized by the return of the diffraction signal corresponding to the uncompressed solid density Si, with some apparent overshoot and ringing.

The Laue signal recorded over the full extent of the Bragg streak shows only a single peak, suggesting that there is no transverse compression. The time-resolved Laue signal is shown in Fig. 11(b). There is no change in the time-resolved Laue signal through the time of shock breakout, suggesting that the Si lattice responds uni-axially on the time scale of the experiment (~5 nanoseconds), even though it is shocked above the HEL. In this case, the time-integrated Bragg signal shows the same two peaks, one corresponding to uncompressed Si, the second to shock compressed Si. Note that for this Si experiment, the shock pressure is only moderately above the HEL compared to the Al hydrodynamics experiment discussed above.

## VIII. SUMMARY

We have demonstrated that high-pressure and high-strain rate solid-state experiments may be done using an intense

laser. By introducing internal shielding in the *Hohlraum* target to prevent x-ray preheat and by shaping the laser pulse to generate a sequence of shocks, a metal foil may be compressed nearly isentropically. An RT instability experiment was conducted using thin Al foils with a pre-imposed modulation at the unstable embedded interface. Measured growth rates are suggestive of a model of shock-induced localized heating in shear bands, followed by conduction of the heat to the bulk sample, and recovery of the material strength. A dynamic diffraction experiment was performed using Si crystals. In separate experiments, the Si crystals were shocked along the (111) lattice direction at up to 33 GPa, and along the (400) direction at 11.5–13.5 GPa. Only a 1D compression was observed above the HEL of 8.4 GPa for Si(400), indicating that the response is uniaxial on the ns time scale.

## ACKNOWLEDGMENTS

The Nova technical staff did an excellent job supporting the complex setup for this experiment. We thank J. Belak for useful discussions regarding this work. This work was performed under the auspices of the United States Department of Energy by the Lawrence Livermore National Laboratory under Contract No. W-7405-48-Eng. The x-ray diffraction experiments were performed on Nova through the Science Use of Nova Program. Additional support was provided by the University of California Materials Research Institute, LLNL.

<sup>1</sup>P. England, and P. Molnar, *Science* **278**, 647 (1997).

<sup>2</sup>D. J. Steinberg and C. M. Lund, *J. Appl. Phys.* **65**, 1528 (1989).

<sup>3</sup>D. J. Steinberg, S. G. Cochran, and M. W. Guinan, *J. Appl. Phys.* **51**, 1498 (1980).

<sup>4</sup>L. C. Chhabildas and J. R. Asay, *J. Appl. Phys.* **50**, 2749 (1979).

<sup>5</sup>J. F. Barnes, P. J. Blewett, R. G. McQueen, K. A. Meyer, and D. Venable, *J. Appl. Phys.* **45**, 727 (1974).

<sup>6</sup>A. I. Lebedev, P. N. Nizovtsev, and V. A. Rayevsky, in the *Proceedings of the 4th International Workshop on the Physics of Compressible Turbulent Mixing*, 29 March–1 April, Cambridge, England (Cambridge University Press, Cambridge, 1993), p. 81.

<sup>7</sup>A. I. Lebedev, P. N. Nizovtsev, V. A. Raevskii, and V. P. Solov'ev, *Dokl. Akad. Nauk* **349** (MAIK Nauka/Interperiodica Publishing, Moscow July 1996), pp. 332–4. Translation: *Phys. Dokl.* **41**, 328 (1996).

<sup>8</sup>E. M. Campbell, J. T. Hunt, E. S. Bliss, D. R. Speck, and R. P. Drake, *Rev. Sci. Instrum.* **57**, 2101 (1986).

<sup>9</sup>H. N. Kornblum, R. L. Kauffman, and J. A. Smith, *Rev. Sci. Instrum.* **57**, 2179 (1986).

<sup>10</sup>G. B. Zimmerman and W. L. Kruer, *Comments Plasma Phys. Control. Fusion* **2**, 51 (1975).

<sup>11</sup>J. A. Moriarty, D. A. Young, and M. Ross, *Phys. Rev. B* **30**, 578 (1984).

<sup>12</sup>P. M. Bell, J. D. Kilkenny, G. Power, R. Bonner, D. K. Bradley, in *Ultra-high Speed and High Speed Photography, Photonics, and Videography '89* (SPIE, Bellingham, WA, 1989), Proc. SPIE Vol. 1155, pp. 430–444.

<sup>13</sup>K. S. Budil, T. S. Perry, P. M. Bell, J. D. Hares, P. L. Miller, T. A. Peyser, R. Wallace, H. Louis, and D. E. Smith, *Rev. Sci. Instrum.* **67**, 485 (1996).

<sup>14</sup>J. W. Miles, Technical Report No. GAMD-7335 (General Dynamics, San Diego, 1966). Copies available from the Defence Technical Information Center, 8725 Kingman Rd., Ft. Belvoir, VA 22060.

<sup>15</sup>D. C. Drucker, *Ingenieur-Archiv* **49**, 361 (1980).

<sup>16</sup>D. E. Grady and J. R. Asay, *J. Appl. Phys.* **53**, 7350 (1982).

<sup>17</sup>V. A. Raevskii, private communication (1999).

<sup>18</sup>E. Zaretzky, *J. Appl. Phys.* **78**, 1 (1995).

<sup>19</sup>Q. Johnson, A. Mitchell, R. N. Keeler, and L. Evans, *Phys. Rev. Lett.* **25**, 1099 (1970); Q. Johnson, A. Mitchell, and L. Evans, *Nature (London)* **231**, 310 (1971).

- <sup>20</sup>J. S. Wark, R. R. Whitlock, A. A. Hauer, J. E. Swain, and P. J. Solone, *Phys. Rev. B* **40**, 5705 (1989).
- <sup>21</sup>A. A. Hauer, J. S. Wark, D. Kalantar, B. Remington, R. Kopp, J. Cobble, B. Failor, G. Kyrala, M. Meyers, R. Springer, and T. Boehly, *Proc. SPIE* **3157**, 72 (1997).
- <sup>22</sup>D. H. Kalantar, E. A. Chandler, J. D. Colvin, R. Lee, B. A. Remington, S. V. Weber, L. G. Wiley, B. H. Failor, A. Hauer, J. S. Wark, A. Loveridge, M. A. Meyers, and G. Ravichandran, *Rev. Sci. Instrum.* **70**, 29 (1999).
- <sup>23</sup>N. C. Woolsey and J. S. Wark, *J. Appl. Phys.* **81**, 3023 (1997).
- <sup>24</sup>N. C. Woolsey, J. S. Wark, and D. Riley, *J. Appl. Crystallogr.* **23**, 441 (1990).
- <sup>25</sup>E. Zaretsky *et al.*, *Sov. Phys. Dokl.* **36**, 76 (1991).
- <sup>26</sup>P. A. Rigg and Y. M. Gupta, *Appl. Phys. Lett.* **73**, 1655 (1998); Y. M. Gupta, K. A. Zimmerman, P. A. Rigg, E. B. Zaretsky, D. M. Savage, P. M. Bellamy, *Rev. Sci. Instrum.* **70**, 4008 (1999).
- <sup>27</sup>B. L. Holian and P. S. Lomdahl, *Science* **280**, 2085 (1998).
- <sup>28</sup>J. Belak, J. N. Glosli, D. B. Boercker, I. F. Stowers, in *Proceedings from Modeling and Simulation of Thin-Film Processing Symposium* (San Francisco, CA, USA, 17–20 April 1995), edited by D. J. Srolovitz and C. A. Volkert (Pittsburgh, PA, USA: Mater. Res. Soc., 1995), pp. 181–90.